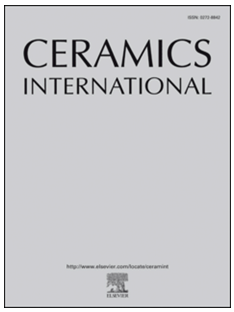

Mechanisms of simultaneously enhanced strength and ductility of titanium matrix composites reinforced with nanosheets of graphene oxides

L.L. Dong, B. Xiao, L.H. Jin, J.W. Lu, Y. Liu, Y.Q. Fu, Y.Q. Zhao, G.H. Wu, Y.S. Zhang

PII: S0272-8842(19)31690-6

DOI: https://doi.org/10.1016/j.ceramint.2019.06.189

Reference: CERI 21998

To appear in: *Ceramics International*

Received Date: 23 March 2019

Revised Date: 1 June 2019

Accepted Date: 18 June 2019

Please cite this article as: L.L. Dong, B. Xiao, L.H. Jin, J.W. Lu, Y. Liu, Y.Q. Fu, Y.Q. Zhao, G.H. Wu, Y.S. Zhang, Mechanisms of simultaneously enhanced strength and ductility of titanium matrix composites reinforced with nanosheets of graphene oxides, *Ceramics International* (2019), doi: https://doi.org/10.1016/j.ceramint.2019.06.189.

Mechanisms of Simultaneously Enhanced Strength and Ductility of Titanium Matrix Composites Reinforced with Nanosheets of Graphene Oxides

L.L. Dong [a], B. Xiao [a, b], L.H. Jin [a], J.W. Lu [a], Y. Liu [a], Y.Q. Fu [c]

Y.Q. Zhao[a], G.H. Wu[d], Y.S. Zhang [e, a *]

[a] Advanced Materials Research Central, Northwest Institute for Nonferrous Metal Research, Xi'an 710016, PR China

[b] School of Materials Science and Engineering, Northwestern Polytechnical University, Xi'an 710072, PR China

[c] Faculty of Engineering and Environment, Northumbria University, Newcastle upon Tyne, NE1 8ST, UK

[d] School of Materials Science and Engineering, Harbin Institute of Technology, Harbin 150001, PR China

[e] Xi'an Rare Metal Materials Institute Co., Ltd, Xi'an, PR China

Abstract:

Types and sizes of nanoparticles as the secondary phases of metal matrix composites (MMCs) significantly affect their microstructures and mechanical properties. In literature, graphene nanoplates (GNPs) have been introduced into Ti matrix composites (TiMCs) but it is still a contradictory issue on how to

* Corresponding author: Professor Y.S. Zhang
E-mail: y.sh.zhang@163.com, y.sh.zhang@c-nin.com (Y.S. Zhang)

simultaneously increase both the strength and toughness of the TiMCs using these graphene nanosheets. In the present work, graphene oxide nanosheets (GONs) were chosen as the reinforcement agent to prepare GONs/Ti matrix composites through a combined process of powder metallurgy and spark plasma sintering (SPS). Microstructures and mechanical properties of the TiMCs were investigated at both room temperature and high temperatures in order to evaluate strengthening and toughening effects of the GONs. It was revealed that 0.2% yield strength and ultimate tensile strength of the Ti-0.6wt% GONs composite were increased by 7.44% and 9.65% as compared to those of pure Ti, though their elongation was slightly decreased to 22.9 %, compared with 31.3% of the pure Ti. All the synthesized samples exhibited typical characteristics of ductile fracture with dimple patterns and pulling-out of the GONs. The Ti-0.6wt% GONs composite demonstrated an enhancement of 31.66% in the 0.2% yield compressive strength measured at a temperature of 700 ^{o}C. Based on both theoretical analysis and experimental verification, the strengthening and toughening mechanisms of the nanocomposites were attributed to the synergistic effects of *in-situ* TiC_x dispersion strengthening from the GONs and effective load transfer capability due to the well-formed interfacial structures.

Keywords: Ti matrix composites, Graphene oxides nanosheets, Mechanical properties, Strengthening mechanism

1. Introduction

Since the first report of graphene (also including graphene nanoplates, GNPs) by Geim and Novoselov in 2004 [1], it has been regarded as the next generation reinforcement material owing to its excellent mechanical [2], electrical [3], and physical-chemical properties [4]. Many researchers have introduced the GNPs and their derivatives into the matrix of metal, ceramics and polymer, and achieved remarkable improvements of their mechanical properties and generation of multi-functionalities [5-12]. For example, Chen et al. [13] reported that 1.2 vol.% graphene/Mg matrix composites exhibited a 78% increase in micro-hardness values compared with that of pure Mg. Dong et al. [14] found that the hardness has been enhanced by up to 121% with only 1.0 wt% graphene being added into the WCu alloy, and simultaneously the electrical conductivity of graphene/WCu composites was significantly increased after 0.5 wt% of graphene was added. Nazeer et al. [15] showed that reduced graphene oxide (rGO) and copper composites achieved a remarkable enhancement of thermal conductivity (348 W/m·K) and hardness (71.2 HV, which is 61% higher than that of pure Cu). Recently, Chu et al havesignificantly enhanced thermal conductivity (525W/m·K) of graphene/copper composites with highly aligned graphene network, which was 50% higher than that of Cu matrix and among the highest values ever reported for the graphene/metal composites [16-17].

Owing to their combined good toughness and remarkable mechanical properties, Ti matrix composites have been attracting extensive attention, especially for aerospace and automobile industries [18-21]. Currently the main focus of this research field is the reduction of fabrication cost or development of novel technologies to

further enhancement their overall properties. In the past a few years, many nano- or micro-particles have been employed to strengthen the Ti matrix composites using various methods [22-26]. For example, Huang et al. [27] fabricated 5 vol.% TiB_w/Ti-6Al-4V matrix composite using a hot pressing reaction sintering process and achieved an ultimate tensile strength (UTS) of 1090 MPa and a poor fracture elongation of 3.6%. Carbon nanotube/titanium (CNT/Ti) composites with a high tensile strength of 872±5 MPa and a elongation of ~0.6% were fabricated using a high pressure torsion in Ref. [28]. However, so far it is still a contradictory issue on how to simultaneously increase both the strength and toughness of Ti matrix composites.

To solve the above-mentioned issue, this work aims at the introduction of graphene oxides nanosheets (GONs) into the pure Ti matrix and sintering of nanocomposites using a ambient temperature hydrothermal synthesis method, followed by spark plasma sintering (SPS) process. The GONs were selected as the resource of graphene material owing to their good dispersability in the aqueous suspension and easy absorption onto the surfaces and interfaces of Ti matrix [29]. The optimum contents of the GONs were determined using results of Vickers hardness, tensile tests and microstructural characterization of the Ti matrix composites. The interfacial structure of the composites was characterized and the corresponding strengthening mechanisms of GONs reinforced Ti matrix were discussed based on both the experimental results and theoretical analysis.

2. Experimental procedure

2.1 Fabrication of GONs /Ti matrix composites

Commercial Ti powders with an average diameter of ~150 μm and a purity of ~99.9% and graphene oxide nanosheets (GONs) were used as source materials. Characterization using atomic force microscope (AFM) (see Fig. 1) shows that the average thickness of the GONs in this work is about 10 nm.

The detailed process of GONs/Ti matrix composites has been previously presented in our work [30]. In this study, the GONs with amounts of 0, 0.3, 0.6 and 0.9 wt% were added into pure Ti matrix composites using the reported ambient temperature hydrothermal synthesis method [30]. The GONs-Ti mixed powders were sintered using SPS at a sintering temperature of ~1100 ^{o}C ($\pm$10 ^{o}C) for 5 min under a pressure of 45 MPa in a vacuum atmosphere.

Fig. 1 (a) 3D atom force microscopy (AFM) image of surface morphology; (b) top-view AFM image of as-received GO; and (c) corresponding cross-section height analysis.

2.2 Characterization of microstructure and mechanical properties

Microstructural evolution and the sintering behavior of the GONs/Ti matrix composites were investigated using a scanning electron microscope (SEM, Zeiss GeminiSEM) and a transmission electron microscope (TEM, JEOL JEM-2100Plus), respectively. For the TEM sample preparation, about 0.2 mm thick GONs/Ti matrix composites flake was obtained using wire-cutting machine, and then mechanically

ground into a thickness of 30~50 μm used metallographic sand paper. Thinning of the sample was carried out using a Gatan PIPS 691 ion milling system and argon ion gun was used in the ion etching process with the accelerating voltage in the range of 2.5–5 keV and an incident angle of in the range of4 to 10^{o}.

Surface morphologies and size of GONs was obtained using an AFM (FastScan, Bruker, Karlsruhe, Germany) in a tapping mode. The GONs in the composites were characterized using Raman spectroscopy (Micro Raman LabRAM VIS-633) with a He-Ne laser beam (532 nm) over the range of 1000~3000 cm^{-1}. X-ray diffraction (XRD, XRD-7000) with Cu-K_{α} radiation source was used to investigate the crystalline phases of samples.

Vickers hardness of samples was measured using a Vickers hardness tester (MVS-1000IMT2) by applying a normal force of 200 g for a fixed duration of 10 s. Each sample was measured at least 5 indentations in order to obtain an average value.

The tensile tests were carried out at room temperature using an Instron 8871 universal testing machine with a strain rate of 1×10^{-3} s^{-1}. The high temperature compression test was performed at 700 ^{o}C using an GLEEBLE3500 testing machine. At least three samples were performed to acquire average tensile and compressive properties. The tensile fracture surface morphologies and compositions were characterized using the SEM equipped with an energy dispersive X-ray spectroscope (EDS).

3. Results analysis and discussions

Fig. 2 shows the SEM images of GONs/Ti matrix composites after SPS process. There are no obvious GONs nanosheets noticed in the composites. Some micro-holes (denoted by green arrows in Fig. 2) were observed after the GONs were used, which is mainly because the thermal expansion coefficients of carbides and Ti matrix or GONs (as the second phases) are mismatched [31]. The only evidence of the existence of GONs visible from the SEM observations is those cracked holes on the surfaces of the samples in Fig. 2(d), which can also be verified using the EDS mapping results shown in Fig. 2(e). A whole piece of GONs can be observed from the fracture morphology analysis. It is noticed that the TiC_x particles (as indicated using red triangle arrows and confirmed by EDS result in Fig. 2(e)) are randomly distributed on the surface of the composites when the GONs content is low, as shown in Figs. 2(b) and 1(c). However, when the 0.9 wt% GONs was added into the Ti matrix composites, the randomly distributed TiC_x particles are observed to link together to form a network, which are *in-situ* formed at interfaces of the Ti boundary grains, as observed in Fig. 2(d).

Fig. 2 SEM images of Ti matrix composites reinforced with different GONs (a) 0 wt%, (b) 0.3 wt%, (c) 0.6 wt% and (d) 0.9 wt%, (f) EDS element analysis of the dark color phase marked in (d), respectively.

Based on the XRD results of SPS processed Ti matrix composites with different GONs contents, the obvious Ti characteristic peaks were detected as shown in Fig.

3(a), but there are no obvious peaks of GONs or rGONs. The main reason may be attributed to the small amount of GONs [32]. From Fig. 3(a), it is noticed that the diffraction peaks are broadened and the intensities are decreased when the GONs were introduced into Ti matrix, which should be attributed to the grain refinement caused by the GONs in metal matrix composites [33-34]. However, weak peak around at $2\theta = \sim 35.2^{o}$ (corresponding to (111) plane of TiC_x) can be observed in Fig. 3(b), and their intensities are increased with an increase of the GONs content, revealing that the Ti reacted with carbon (i.e. GONs) to form TiC_x phase during the SPS process.

Raman spectroscopy analysis results of the composites are shown in Fig. 3(c). There are two obvious characteristic peaks of the GONs, i.e. D band (1350 cm^{-1}, the defect band), G band (1591 cm^{-1}), as observed in Fig. 3(c). However, an obvious peaks at 2692 cm^{-1} (2D band) for SPS sintered 0.6wt.% GONs/TiMCs was clearly detected, revealing that the GONs was reduced into graphene during the SPS [14]. Generally, the existence of 2D peak is often used to confirm the presence of graphene and determine the number of graphene layers. For a single layer of graphene, the 2D peak is quite narrow and relatively sharp, however it becomes broadened and displays peak-splitting with an increase in the number of graphene layers [35]. Based on these results, the multilayer GNPs exist in the SPS processed samples.

The intensity ratio of the D band and G band is often used to evaluate the defects and quality of the carbon materials. However, in order to precisely estimate defect and structure of GONs in this work, we calculated the value of I_D/I_G using Gauss area numerical integration method and the results are shown in Fig. 3(c). We have found

that the ratios of I_D/I_G are changed (an increase of 52.1%) before (0.69) and after SPS (1.05) for the TiMCs, which means that there are significant damage of the GONs structure after the SPS process. A detailed observation can be seen in Figs. 4 to 6. Furthermore, the intensity of G peak becomes broadened after the SPS, which are attributed to the large compressive stress generated in the GNOs/TiMCs during SPS [36].

Fig. 3(a) XRD pattern and (b) enlarged region at $2\theta = 35.0\sim36.0^{o}$ of SPS Ti matrix composites containing different GONs contents, (c) the Raman spectrum of GONs and SPS 0.6wt% GONs/Ti matrix composites.

The hardness of the samples is increased from 181.3 HV (pure Ti) to 203.8 HV (for the sample with 0.3wt% GONs addition), which is ~ 12.4% enhancement owing to a small number of GONs addition, as listed in Table 1. The main reasons for this significant enhancement in the hardness are:

(1) The GONs was partially reduced into reduced GONs during the SPS, and the Ti grains were refined by the nano- reduced GO sheets [37];

(2) According to the mixture rule of composites, the addition of reduced GONs or graphene nanosheets with high hardness and strength results in the increase of hardness of composites;

(3) A well-dispersed GONs/Ti interface was obtained owing to the formation of small number of TiC_x.

However, we have found that if the GONs addition was increased over 0.6 wt%,

there was a decrease of hardness from 212.9 HV to 211.4 HV. These results are in good agreements with those reported for the graphene reinforced with Al matrix composites [38-39]. In fact, an enhancement in hardness can result in an improvement in wear and scratch resistance of Ti matrix composites, which contributes for a wide range applications of Ti matrix composites materials in applications such as orthopedic implants.

Table 1 Micro-hardness of GONs/Ti matrix composites sintered at 1100 ^{o}C.

Fig. 4 present the TEM images of the 0.3 wt% GONs/Ti matrix composites. As shown in Fig. 4(a), the GONs with a length of 800 nm and width of 200 nm are observed on the surface of the Ti grains. The selected area diffraction pattern (SADP) in Fig. 4(b) show strong diffraction patterns from titanium matrix, which overshadows the weak diffraction from the contaminated GONs. We can also observe that the GONs show an amorphous structure according to the SADP. Chu et al. [14] reported that the transformation of the amorphous carbon from graphene and its derivate can enhance the interfacial bonding between the graphene and metal matrix through *in-situ* formation of the carbide nanolayers. However, there are no obvious TiC_x particles or nanolayers observed in Fig. 4(a) owing to the lower contents of the GONs.

Fig. 4(a) TEM image and (b) the selected area diffraction pattern (SADP) of 0.3wt% GONs/Ti matrix composites.

In order to further investigate the influence of GONs on the microstructure and interfacial structure, the TEM images and EDS mapping results of 0.9 wt% GONs/Ti matrix composites were obtained and the results are displayed in Fig. 5. These images revealed that there are two types of second phase particles located at the grain boundaries of the Ti matrix, i.e. clubbed shape (Fig. 5(a)) and axiolitic shape (Fig. 5(b)). Fig. 5(c) is the selected area electron diffraction (SEAD) pattern collected from the second phase particles, which can be identified as face-centered cubic (FCC) structure of TiC according to the crystallographic calibration.

The standard free energy (ΔG) of TiC formation by reaction between carbon source and Ti can be written as [30]:

$$\Delta G=-184571.8+41.382T-5.042TlnT+2.425\times10^{-3}T^{2}-9.79\times10^{5}/T \quad (T<1939K) \quad (1)$$

where ΔG (kJ/mol) is the free energy, T (K) is the reaction temperature. According to Eq. (1), the ΔG value of TiC formation at 1100 ^{o}C in this work is -157.75 kJ/mol, which is below zero. This suggested that *in-situ* reaction formation of TiC_x is spontaneous, further explaining the microstructural analysis shown in Fig. 2.

Fig. 5(a) and (b) TEM, EDS mapping and (c) Selected area diffraction pattern images of 0.9 wt% GONs/Ti matrix composites fabricated by SPS process. (a) and (b) show there are two types of TiC_x particles embedded in the Ti matrix.

Fig. 6 shows the detailed interfacial characteristics of 0.9 wt% GONs/Ti matrix

composites characterized using TEM. No obvious micro-cracks, impurities and porosities can be observed at the interfaces as shown in Fig. 6(a) and (b), revealing that a good interfacial bonding was formed. Fast Fourier transform (FFT) and inverse Fast Fourier transform (IFFT) were then used to investigate the selected regions near or at the interface of the GONs-Ti, and the corresponding results are presented in Figs. 6(c) and 6(d). For region A in Fig. 6(c), the FFT shows an amorphous ring, which correspond to the characteristic (002) diffraction spots of C (i.e. GONs). According to the noise-filtered IFFT image, the lattice inter-planar spacing was measured to be about 0.3515 nm, which means that it is near the monolayer structure of the GO sheets [40]. This shows the GO has an amorphous structure in this work owing to the high pressure and high temperature used in the SPS [41]. As for region B in Fig. 6(d), (100) and (01-1) diffraction patterns with the lattice spacing of ~0.24 nm were observed, which are corresponding to the Ti5C8 interfacial layers (confirmed by PDF # 72-2496). This means the active carbon atoms from GONs react with Ti matrix. Fig. 6(e) is the SAED image of the region C, identifying as Ti crystal along the [011] direction on the basis of a close-packed hexagonal unit cell.

Fig. 6 Detailed analysis and characteristic of interface between Ti matrix and GONs (a) TEM image of GONs/Ti matrix composites, (b) enlarged view image of blue rectangle in (a), (c) and (d) FFT, IFFT and corresponding lattice spacing measurement recorded at the marked A, B regions in (b), respectively, (e) SAED of C region in (b).

In order to analyze the effect of GONs addition on the mechanical properties of

the Ti matrix composites, room temperature tensile tests were carried out (Fig. 7(a)) and the results are shown in Figs. 7(b) and (c). The 0.2% yield strength (YS) and ultimate tensile strength (UTS) of the SPS processed 0.6wt.% GONs/Ti matrix composites in Fig. 7(b) are 433 MPa and 545 MPa, respectively. These values are superior to those of the pure Ti (YS=403 MPa, UTS=497 MPa), and are increased by about 7.44% and 9.65%, respectively. As shown in Fig. 7(b), the content of GONs shows insignificant enhancing effect on the UTS and YS of the composites when the GONs contents are over 0.6 wt.%. However, the introduction of GONs slightly deteriorates the ductility of the composites, as shown in Fig. 7(c), i.e. the elongation of the samples is decreased from 31.3% (pure Ti) to 20.1% when the 0.9 GONs wt.% was added.

The enhancement of the mechanical properties, in particular the UTS of the Ti matrix composites can be attributed to the effects of grain size [42], solid solution of carbon [43-44] and TiC_x second phase including the remained GONs. In fact, the *in-situ* formation of TiC_x particles can retard the Ti grain growth and improve the strength of the materials by pinning and dispersion strengthening mechanisms during the process of tensile or compression. On the other hand, the physical properties of TiC_x itself (high Young's modulus) would increase the hardness and strength of the Ti matrix composites. However, the elongation of GONs/Ti matrix composites are all lower than that of pure Ti, which are attributed to the existence of the formation sites of crack which can initiate between TiC_x particles and Ti matrix during the tensile deformation. In this work, the reaction between the GONs and Ti matrix might not be

totally incompleted due to the short sintering time, thus resulting in the presence of the residual carbon and TiC_x particles. As a result, the pores would form between the Ti grains by weak bonding owing to the different CTEs (i.e. coefficients of thermal expansion) between TiC_x particles and Ti matrix, which decrease the ductility of the composites.

Fig. 7 Room temperature engineering tensile-strain curves and (b) ~ (c) corresponding tensile properties of Ti matrix composites addition of different GONs.

Fig. 8 shows the high temperature compressive properties of Ti matrix composites reinforced with GONs tested at 700 ^{o}C. Obviously, the addition of the GONs plays a significant role in influencing the compressive properties of samples as shown in Fig. 8(a). As seen from Fig. 8(b), the compressive strength increases firstly but then decreases. The Ti matrix composites show a maximum value of 0.2% yield compressive strength of 75.77±1.82 MPa when the GONs have a content of 0.6wt.%, which is about 31.66% enhancement as compared to that of the pure Ti with a value of 57.55±1.53 MPa. The presence of large mass fraction of GONs (over 0.6 wt%) in the Ti matrix results in the low compressive strength (Fig. 2(d)). This result is well agreed with those reported by Su et al [45].

Fig. 8 (a) True stress-strain curves and (b) corresponding compressive strength of GONs/Ti matrix composites compressed tested at 700 ^{o}C.

SEM fracture images of Ti matrix composites with different GONs contents are shown in Fig. 9. As can be seen from Fig. 9(a), the pure Ti materials exhibits ductile fracture characteristics with lots of dimples. It is interesting to see that all the samples show the typical dimple patterns, the characteristics of a ductile fracture. Compared Figs. 9(a) and 9(d), the GONs shows an apparent reinforcement in metal matrix composites. When the GONs is 0.9 wt%, cracks and holes can be found around the Ti grains on the fracture surface as shown in Fig. 9(d), owing to the large differences of CTEs between the GONs and Ti matrix [46]. This has thus resulted in the decrease of the elongation (CTE_{Ti}=8.5 $\times$ 10^{-6} K^{-1}[47], CTE_{TiCx}= 6.5~7.0 $\times$ 10^{-6} K^{-1} [48], CTE_{GONs}= 0.9~1.2$\times$$10^{-6}$ K^{-1}[49]). On the other hand, there are many shear bands and tearing ridges clearly observed in Fig. 9(d). It is worthwhile to note that curly GO nanosheets are still well-maintained as shown by the blue arrow in Fig. 9(d). As seen in Fig. 9(d), some of the GONs are pulled out from the composites. Residual GO nanosheets can enhance the effective load transfer during tensile test [50]. The fractured morphology analysis is in accordance with tensile properties results in Fig. 7.

Fig. 9 SEM tensile fractographs of GONs/Ti matrix composites at different magnification. (a) 0 wt%, (b) 0.3 wt%, (c) 0.6 wt% and (d) 0.9 wt%, respectively.

The effect of GONs addition on the mechanical properties of Ti matrix composites could be considered as a synergistic effect of the grain refinement (Fig. S1)

and reinforcement of reduced GONs. According to Hall-Petch formula, the enhanced 0.2% YS of metal matrix composites by grain refinement ($\Delta\sigma_{GR}$) can be written as follows [42]:

$$\Delta\sigma_{GR} = K(D_c^{-0.5} - D_m^{-0.5}) \quad (2)$$

where K is the Halle-Petch coefficient, and usually shows the average effect of the grain boundaries in the polycrystal, K=0.68 MPa·m$^{1/2}$ [51], D_c and D_m are the average sizes of rGO/Ti and pure Ti, respectively. For 0.6 wt% GONs addition, $\Delta\sigma_{GR}$ is calculated to be 20.5 MPa, which is much lower than that the observation in Fig. 7(b).

On the other hand, some intact GONs are maintained after the SPS process. Especially, they are embedded around the grain boundaries of Ti particles. Based on the modified shear lag model [52-53], the 0.2% yield strength $\Delta GONs$ of GONs effect can be expressed as:

$$\Delta GONs = \frac{\sigma_m \cdot V_{GONs}(\lambda - 4)}{4} \quad (3)$$

where σ_m is the 0.2% YS of the Ti matrix (403 MPa in this work), V_{GONs} is the volume fraction of GONs, λ is the aspect ratio of GONs (the diameter and thickness of GONs are 500 nm and 10 nm (Fig. 1), respectively, and λ is estimated to be ~ 50).

Hence, the V_{GONs} can be expressed using Equations (4):

$$V_{GONs} = \frac{(1-\omega)m_{GONs}}{(1-\omega)m_{GONs} + \frac{\rho_{GONs}}{\rho_{Ti}} \cdot (100 - (1-\omega)m_{GONs})} \quad (4)$$

in which ω is the volume fraction of GONs with Ti, the m_{GONs} is the mass fraction

of GONs addition in Ti matrix composites (here, m_{GONs}=0.6), ρ_{GONs} (2.2 g/cm^3 [7]) and ρ_{Ti} (4.8g/cm^3) are theoretical density of GONs and Ti, respectively.

Combination of Eqs. (3) and (4), the $\Delta GONs$ can be estimated using Eq. (5):

$$\Delta GONs = \frac{20150}{1+0.458\cdot(\frac{100}{(1-\omega)\cdot 0.3}-1)} \quad (5)$$

In Eq. (5), $\frac{100}{(1-\omega)\cdot 0.3}-1>>0$ for the $0<\omega<1$, so the Eq. (5) can be rewritten as:

$$\Delta GONs = \frac{20150}{1+\frac{152.67}{1-\omega}} \quad (6)$$

Of course, some GONs are reacted with Ti matrix to formed TiC_x during the SPS according to SEM results and our previous work [29]. The nano/submicron TiC_x particles will play a key role in the significant strengthening. The Orowan strengthening of 0.2% YS by TiC_x (ΔTiC_x) can be calculated using the Orowan-Ashby model [54]:

$$\Delta TiC_x = \frac{MGb}{2.36\pi}\cdot\ln(\frac{d}{2b})\cdot\frac{1}{\lambda-d} \quad (7)$$

where M (=3.1) is the Taylor factor, G is the shear modulus (= ~45 GPa), b is the burgers vector (= 0.289 nm) and d is the equivalent diameter of TiC_x (for axiolitic shape TiC_x, d=1 μm estimated from Fig. 5(b)), λ is the inter-planar spacing of TiC_x ($\lambda = d\sqrt{\frac{\pi}{6V_{TiCx}}}$ [55-56]).

As mentioned in Eq. (4), V_{TiCx} can also be expressed as Eq. (8):

$$V_{TiCx} = \frac{2.24\omega m_{GONs}}{2.24\omega m_{GONs} + \frac{\rho_{GONs}}{\rho_{TiCx}} \cdot (100 - 2.24\omega m_{GONs})} \quad (8)$$

The density of TiC_x is 4.9 g/cm^3 [57]. As a result, the strengthening effect of TiC_x can be evaluated using Eq. (9)

$$\Delta TiC_x = \frac{40.563}{\sqrt{\frac{196.8}{\omega} - 7.16} - 1} \quad (9)$$

Because $\sqrt{\frac{196.8}{\omega} - 7.16} >> \sqrt{\frac{196.8}{\omega}}$ when $0 < \omega < 1$, the Eq. (9) can be simplified as Eq. (10):

$$\Delta TiC_x = \frac{40.563}{\sqrt{\frac{196.8}{\omega}} - 1} \quad (10)$$

Combining Eqs. (6) and (10), the strengthening effects of GONs and TiC_x in this work can be expressed using:

$$\Delta\sigma_{combine} = \frac{20150}{1 + \frac{152.67}{1-\omega}} + \frac{40.563}{\sqrt{\frac{196.8}{\omega}} - 1} \quad (11)$$

Previous studies on identifying the contribution of carbon solid solution interstitial atoms in Ti matrices proved that solubility of carbon in α-Ti is only 0.05 wt% [25]. Solid solution strengthening by carbon interstitial atoms contributes up to 7 MPa per 0.1 wt% carbon. In addition of solid solution strengthening of TMCs by carbon atoms, Ti matrices have higher affinity towards oxygen (O_2) and nitrogen (N) atoms during the powder metallurgy processing [54]. In these studies, it was proposed that solid solution strengthening by interstitial O and N atoms in TiMCs have a reinforcement effect as 769 MPa/ increased mass% and 1146 MPa/ increased mass%,

respectively.

The theoretical strengthening effects of GONs, TiC_x and their combined results in Ti matrix composites are shown in Fig. 10. If the GONs have not reacted with Ti matrix, the strengthening effect is only caused by the GONs, with a value of 131 MPa. However, if the GONs are reacted with Ti matrix completely, the strength calculated is about 512 MPa owing to the presence of TiC_x. In fact, in this work, some of the GONs are reacted with Ti matrix owing to the advantage of SPS (i.e. short time, high temperature and high efficiency). Recently, we have successfully fabricated the large scale and homogeneous metallic nano-particles coated reduced graphene oxides or graphene nanoplates at room temperature [14, 58]. We believe that the interfacial structure of GONs/Ti matrix composites could be further optimized and thus could maximize the strengthening effect of graphene and its derivates.

Fig. 10 The theoretical calculated strengthening effects of GONs, TiC_x and their combined result versus the reaction fraction of GO with Ti during SPS.

4. Conclusions

In this work, the Ti matrix composites reinforced with different GONs contents were fabricated using the SPS process operated at the temperature of 1100 ^{o}C and a pressure of 45 MPa. The 0.6 wt.% GONs/Ti matrix composites achieved superior mechanical properties, including high hardness of 212.9 HV (~ 17.4% rise), outstanding 0.2% YS of 433 MPa (7.44% rise) and UTS of 545 MPa (9.65% rise), as

well as good elongation of 22.9%. Also, Ti-0.6wt% GONs composites demonstrated 31.66% enhancement in the 0.2% yield compressive strength at 700 ^{o}C. Moreover, there are two types of *in-situ* formed TiC_x second phase particles, i.e. clubbed shape and axiolitic shape, located at the Ti grain boundaries. At the same time, a small number of the TiC_x nanolayers play a significant role in the good interfacial bonding of Ti-Ti grains. The theoretical calculations show that the strengthening mechanism are synergistic effects of *in-situ* TiC_x dispersion strengthening, GONs, and interfacial transfer loading.

Author contributions

Y.S. Zhang, Y.Q. Zhao and G.H. Wu supported and assisted in supervision on the project. L.L. Dong planned and supervised the project. L.L. Dong and B. Xiao performed the experiments. Y. Liu and J.W. Lu made the microstructure characterization and phase structure, and L.L. Dong and L.H. Jin analyzed the SEM fracture. Y.Q. Fu involved in the data analysis and discussions. L.L. Dong analyzed data and wrote the manuscript, and all the authors modified and corrected the manuscript.

Acknowledgements

This work was supported by the National Security Major Basic Research Plan of China and the funded by Northwest Institute for Nonferrous Metal Research (K1652-1, K1652-12, K1740), National Natural Science Foundation of China (Grant

No. U1737108), the Natural Science Basic Research Plan in ShaanXi Province of China (2017ZDJC-19), Innovation Team in Key Areas of Shaanxi Province (2016KCT-30), Key Research and Development Projects of Shaanxi Province (No. 2019GY-164), and Science and Technology Project of Weiyang District of Xi'an City (2018057).

References

[1] K.S. Novoselov, A.K. Geim, S.V. Morozov, D. Jiang, Y. Zhang, S.V. Dubonos, I.V. Grigorieva, A.A. Firsov, Electricfield effect in atomically thin carbon films, Science 306 (2004) 666–669.

[2] C. Lee, X. Wei, J.W. Kysar, J. Hone, Measurement of the elastic properties and intrinsic strength of monolayer graphene, Science 321 (2008) 385–388.

[3] X.B. Fan, W.C. Peng, Y. Li, X.Y. Li, S.L. Wang, G.L. Zhang, F.B. Zhang, Deoxygenation of exfoliated graphite oxide under alkaline conditions: a green route to graphene preparation, Adv. Mater. 20 (2008) 4490–4493.

[4] A.A. Balandin, S. Ghosh, W. Z. Bao, I. Calizo, B. Teweldebrhan, F. Miao, C.N. Lau, Superior thermal conductivity of singer – layer graphene, Nano Lett. 8(3) (2008) 902–907.

[5] J.R. Potts, D.R. Dreyer, C.W. Bielawski, R.S. Ruoff, Graphene-based polymer nanocomposites, Polymer 52 (2011) 5–25.

[6] J. Liu, U. Khan, J. Coleman, B. Fernandez, P. Rodriguez, S. Naher, D. Brabazon, Graphene oxide and graphene nanosheet reinforced aluminium matrix composites: powder synthesis and prepared composite characteristics, Mater. Des. 94 (2016) 87–94.

[7] L.L. Dong, W.G. Chen, C.H. Zheng, N. Deng, Microstructure and properties characterization

of tungsten-copper composite materials doped with graphene, J. Alloy. Compd. 695 (2017) 1637–1646.

[8] M. Tabandeh-Khorshid, J.B. Ferguson, B.F. Schultz, C.S. Kim, K. Cho, P.K. Rohatgi, Strengthening mechanisms of grapheme – and Al_2O_3 reinforced aluminum nanocomposites synthesized by room temperature milling, Mater. Des. 92 (2015) 79–87.

[9] D. Lin, C.R. Liu, G.J. Cheng, Single-layer graphene oxide reinforced metal matrix composites by laser sintering: Microstructure and mechanical property enhancement, Acta Mater. 80 (2014) 183–193.

[10] W.X. Hou, Y. Gao, J. Wang, D.J. Blackwood, S. Teo, Nanodiamond decorated graphene oxide and the reinforcement to epoxy, Compos. Sci. Technol. 165 (2018) 9–17.

[11] K. Chu, J. Wang, Y.P. Liu, Y.B. Li, C.C. Jia, H. Zhang, Creating defects on graphene basal-plane toward interface optimization of graphene/CuCr composites, Carbon 143 (2019) 85-96.

[12] K. Chu, F. Wang, X.H. Wang, D.J. Huang, Anisotropic mechanical properties of graphene/copper composites with aligned graphene, Mater. Sci. Eng. A 713 (2018) 269-277.

[13] L.Y. Chen, H. Konishi, A. Fehrenbacher, C. Ma, J.Q. Xu, H. Choi, H.F. Xu, F.E. Pfefferkorn, X.C. Li, Novel nanoprocessing route for bulk graphene nanoplatelets reinforced metal matrix nanocomposites, Scr. Mat. 67 (2012) 29–33.

[14] W.G. Chen, L.L. Dong, J.J. Wang, Y. Zuo, S.X. Ren, Y.Q. Fu, Synergistic enhancing effect for mechanical and electrical properties of tungsten copper composites using spark plasma infiltrating sintering of copper coated graphene, Sci. Rep. – UK 7 (2017) 17836–17845.

[15] F. Nazeer, Z. Ma, L.H. Gao, F.C. Wang, M.A. Khan, A. Malik, Thermal and mechanical

properties of copper-graphite and copper-reduced graphene oxide composites, Compos. Part B 163 (2019) 77–85.

[16] K. Chu, X.H. Wang, F. Wang, Y.B. Li, D.J. Huang, H. Liu, W.L. Ma, F.X. Liu, H. Zhang, Largely enhanced thermal conductivity of graphene/copper composites with highly aligned graphene network, Carbon 127 (2018) 102-112.

[17] K. Chu, X.H. Wang, Y.B. Li, .J. Huang, Z.R. Geng, X.L. Zhao, H. Liu, H. Zhang, Thermal properties of graphene/metal composites with aligned graphene, Mater. Des. 140 (2018) 85–94.

[18] C. Veiga, J.P. Davim, A.J.R. Loureiro, Properties and applications of titanium alloys: a brief review, Rev. Adv. Mater. Sci. 32 (2012) 133–148.

[19] A. Stanley, S.M. Abkowitz, H. Fisher, P.J. Schwartz, Cerme Ti ® discontinuously reinforced Ti–matrix composites: manufacturing, properties and applications, JOM 56 (2004) 37–41.

[20] S. Moniri Javadhesari, S. Alipour, M.R. Akbarpour, Microstructural characterization and enhanced hardness, wear and antibacterial properties of a powder metallurgy SiC/Ti-Cu nanocomposite as a potential material for biomedical applications, Ceram. Int. 45 (2019) 10603–10611

[21] N. Sadeghi, H. Aghajani, M.R. Akbarpou, Microstructure and tribological properties of in-situ TiC-C/Cu nanocomposites synthesized using different carbon sources (graphite, carbon nanotube and graphene) in the Cu-Ti-C system, Ceram. Int. 44 (2018) 22059–22067.

[22] Z. Yan, F. Chen, Y. Cai, Y. Zheng, Microstructure and mechanical properties of in-situ synthesized TiB whiskers reinforced titanium matrix composites by high-velocity compaction, Powder Technol. 267 (2014) 309–314.

[23] S.D. Luo, Q. Li, J. Tian, C. Wang, M. Yan, G.B. Schaffer, M. Qian, Self-assembled, aligned

TiC nanoplatelet-reinforced titanium composites with outstanding compressive properties, Scr. Mat. 69 (2013) 29–32.

[24] E. Lascoste, C. Arvieu, J.M. Quenisset, Correlation between microstructures of SiC reinforced titanium matrix composite and liquid route processing parameters, J. Mater. Sci. 50 (2015) 5583–5592.

[25] S.F. Li, B. Sun, H. Imai, T. Mimoto, K. Kondoh, Powder metallurgy titanium metal matrix composites reinforced with carbon nanotubes and graphite, Compos. Part A 48 (2013) 57–66.

[26] J.J. Sha, J. Li, S.H. Wang, Z.F. Zhang, Y.C. Wang, J.X. Dai, Microstructure and mechanical properties of hot-pressed ZrC–Ti–CNTs composites, Mater. Des. 107 (2016) 520–528.

[27] L.J. Huang, L. Geng, A.B. Li, F.Y. Yang, H.X. Peng, In situ TiB_w/Ti–6Al–4V composites with novel reinforcement architecture fabricated by reaction hot pressing, Scr. Mat. 60 (2009) 996–999.

[28] F.X. Lia, P.D. Hao, J.H. Yi, Z. Chen, K.G. Prashanth, T. Maity, J. Eckert, Microstructure and strength of nano-/ultrafine-grained carbon nanotube-reinforced titanium composites processed by high-pressure torsion, Mater. Sci. Eng. A 722 (2018) 122–128.

[29] L.L. Dong, W.T. Huo, M. Ahangarkani, B. Zhang, Y.Q. Zhao, Y.S. Zhang, Microstructural evaluation and mechanical properties of in-situ WC/W-Cu composites fabricated by rGO/W-Cu spark plasma sintering reaction, Mater. Des. 160 (2018) 1196–1207.

[30] L.L. Dong, B. Xiao, Y. Liu, Y.L. Li, Y.Q. Fu, Y.Q. Zhao, Y.S. Zhang, Sintering effect on microstructural evolution and mechanical properties of spark plasma sintered Ti matrix composites reinforced by reduced graphene oxides, Ceram. Int. 44 (2018) 17835–17844.

[31] Y.K. Chen, X. Zhang, E.Z. Liu, C.N. He, C.S. Shi, J.J. Li, P. Nash, N.Q. Zhao, Fabrication of in-situ grown graphene reinforced Cu matrix composites, Sci. Rep. -UK 6 (2016) 19363–19671.

[32] X. Feng, J.H. Sui, Y. Feng, W. Cai, Preparation and elevated temperature compressive properties of multi-walled carbon nanotube reinforced Ti composites, Mater. Sci. Eng. A 527 (2010) 1586–1589.

[33] Z.R. Hu, G.Q. Tong, D. Lin, Q. Nian, J.Y. Shao, Y.W. Hu, M. Saei, S.Y. Jin, G.J. Cheng, Laser sintered graphene nickel nanocomposites, J. Mater. Process. Tech. 231 (2016) 143–150.

[34] Y.Z. He, F. Huang, H. Li, Y.W. Sui, F.X. Wei, Q.K. Meng, W.M. Yang, J.Q. Qi, Tensile mechanical properties of nano-layered copper/graphene composite, Physica E 87 (2017) 233–236.

[35] L.L. Dong, W.T. Huo, M. Ahangarkani, B. Zhang, Y.Q. Zhao, Y.S. Zhang, Microstructural evaluation and mechanical properties of in-situ WC/W-Cu composites fabricated by rGO/W-Cu spark plasma sintering reaction, Mater. Des. 160 (2018) 1196–1207.

[36] K. Chu, F. Wang, Y.B. Li, X.H, Wang, D.J. Huang, Z.R. Gen, Interface and mechanical/thermal properties of graphene/copper composite with Mo_2C nanoparticles grown on graphene, Compos. Part A 109 (2018) 267–279.

[37] S. Yi, G.X. Li, S.L. Ding, J. Mo, Performance and mechanisms of graphene oxide suspended cutting fluid in the drilling of titanium alloy Ti-6Al-4V, J. Manuf. Process. 29 (2017) 182–193.

[38] A. Bishta, M. Srivastava, R.M. Kumar, I. Lahiri, D. Lahiri, Strengthening mechanism in graphene nanoplatelets reinforced aluminum composite fabricated through spark plasma sintering, Mater. Sci. Eng. A 695 (2017) 20–28.

[39] K.S. Reddy, D. Sreedhar, K.D. Kumar, G.P. Kumar, Role of reduced graphene oxide on mechanical-thermal properties of aluminum metal matrix nanocomposites, Mater. Today Proc. 2 (2015) 1270–1275.

[40] Y.L. Xue, W.G. Chen, J.J. Wang, L.L. Dong, Q. Zhao, Y.Q. Fu, Formation mechanism and

cohesive energy analysis of metal-coated graphene nanocomposites using in-Situ co-reduction method, Materials 11 (2018) 2071–2189.

[41] A. Nieto, D. Lahiri, A. Agarwal, Synthesis and properties of bulk graphene nanoplatelets consolidated by spark plasma sintering, Carbon 50 (2012) 4068–4077.

[42] X.N. Mu, H.N. Cai, H.M. Zhang, Q.B. Fan, F.C. Wang, Z.H. Zhang, Y.X. Ge, R. Shi, Y. Wu, Z. Wang, D.D. Wang, S. Chang, Uniform dispersion and interface analysis of nickel coated graphene nanoflakes/ pure titanium matrix composites, Carbon 137 (2018) 146–155.

[43] V.C. Nardone, K.M. Prewo, On the strength of discontinuous silicon carbide reinforced aluminum composites, Scripta Metall. 20 (1986) 43–48.

[44] W.J. Kim, S.H. Lee, High temperature deformation behavior of carbon nanotube (CNT) reinforced aluminum composites and prediction of their high temperature strength, Compos. Part A 67 (2014) 308–315.

[45] Y. Su, Q. Zuo, G. Yang, Y. Yang, C. Wei, L. Wang, J. Liu, Compressive properties of the graphene reinforced titanium composites, Rare Metal Mat. Eng. 46(12) (2017) 3382-3386.

[46] N. Sadeghi, M.R. Akbarpour, H. Aghajani, A novel two-step mechanical milling approach and in-situ reactive synthesis to fabricate TiC/Graphene layer/Cu nanocomposites and investigation of their mechanical properties, Mater. Sci. Eng. A 734 (2018) 164–170.

[47] D. Low, T. Sumii, M. Swain, Thermal expansion coefficient of titanium casting, J. Oral Rehabil. 28 (2001) 239–242.

[48] F.X. Li, P.D. Hao, J.H. Yi, K.G. Prashanth, T. Maity, J. Eckert, Strengthening effects in nano-/ultrafine-grained carbon nanotube reinforced-titanium composites investigated by finite element modeling, Metall. Mater. Trans. A 49(2) (2018) 6469–6478.

[49] R.J. Arsenault, N. Shi, Dislocation generation due to differences between the coefficients of thermal expansion, Mater. Sci. Eng. 81 (1986) 175–187.

[50] M. Yang, L. Weng, H.X. Zhu, T.X. Fan, D. Zhang, Simultaneously enhancing the strength, ductility and conductivity of copper matrix composites with graphene nanoribbons, Carbon 118 (2017) 250–260.

[51] Z.R. Hu, F. Chen, J.L. Xu, Z.W. Ma, H.F. Guo, C.J. Chen, Q. Nian, X.N. Wang, M. Zhang, Fabricating graphene-titanium composites by laser sintering PVA bonding graphene titanium coating: Microstructure and mechanical properties, Compos. Part B 134 (2018) 133–140.

[52] J.L. Song, W.G. Chen, L.L. Dong, J.J. Wang, N. Deng, An electroless plating and planetary ball milling process for mechanical properties enhancement of bulk CNTs/Cu composites, J. Alloy. Compd. 720 (2017) 54–62.

[53] P.Z. Shao, W.S. Yang, Q. Zhang, Q.Y. Meng, X. Tan, Z.Y. Xiu, J. Qiao, Z.H. Yu, G.H. Wu, Microstructure and tensile properties of 5083 Al matrix composites reinforced with graphene oxide and graphene nanoplates prepared by pressure infiltration method, Compos. Part A 109 (2018) 151–162.

[54] K. Vasanthakumar, N.S. Karthiselva, Niraj M. Chawake, Srinivasa Rao Bakshi, Formation of TiC_x during reactive spark plasma sintering of mechanically milled Ti/carbon nanotube mixtures, J. Alloy. Compd. 709 (2017) 829–841.

[55] H.P. Zhang, C. Xu, W.L. Xiao, K. Ameyama, C. Ma, Enhanced mechanical properties of Al5083 alloy with graphene nanoplates prepared by ball milling and hot extrusion, Mater. Sci. Eng. A 658 (2016) 8–15.

[56] B. Chen, S. Li, H. Imai, L. Jia, J. Umeda, M. Takahashi, K. Kondoh, Load transfer

strengthening in carbon nanotubes reinforced metal matrix composites via in-situ tensile tests, Compos. Sci. Technol. 113 (2015) 1–8.

[57] L. Cheng, Z. Xie, G. Liu, Spark plasma sintering of TiC ceramic with tungsten carbide as a sintering additive, J. Eur. Ceram. Soc. 33 (2013) 2971-2977.

[58] L.L. Dong, Y.C. Ding, W.T. Huo, W. Zhang, J.W. Lu, Y.Q. Zhao, G.H. Wu, Y.S. Zhang, A green and facile synthesis for rGO/Ag nanocomposites using one-step chemical co-reduction route at ambient temperature and combined first principles theoretical analyze, Ultrason. Sonochem. 53 (2019) 152-163.

List of figure captions:

Fig. 1 (a) 3D atom force microscopy (AFM) image of surface morphology; (b) top-view AFM image of as-received GO; and (c) corresponding cross-section height analysis.

Fig. 2 SEM images of Ti matrix composites reinforced with different GONs (a) 0wt%, (b) 0.3wt%, (c) 0.6wt% and (d) 0.9wt%, (f) EDS element analysis of the dark color phase marked in (d), respectively.

Fig. 3 (a) XRD pattern and (b) enlarged region at $2\theta = 35.0\sim36.0^{o}$ of SPSed Ti matrix composites containing with different GONs, (c) the Raman spectrum of GONs and SPS GONs/Ti matrix composites.

Fig. 4 (a) TEM image and (b) the selected area diffraction pattern (SADP) of 0.3wt% GONs/Ti matrix composites.

Fig. 5 (a) and (b) TEM, EDS mapping and (c) Selected area diffraction pattern images of 0.9 wt% GONs/Ti matrix composites fabricated by SPS process. (a) and (b) show there are two types of TiC_x particles embedded in the Ti matrix.

Fig. 6 Detailed analysis and characteristic of interface between Ti matrix and GONs (a) TEM image of GONs/Ti matrix composites, (b) enlarged view image of blue rectangle in (a), (c) and (d) FFT, IFFT and corresponding lattice spacing measurement recorded at the marked A, B regions in (b), respectively, (e) SAED of C region in (b).

Fig. 7 Room temperature engineering tensile-strain curves and (b) corresponding tensile properties of Ti matrix composites addition of different GONs.

Fig. 8 (a) True stress-strain curves and (b) corresponding compressive strength of Ti

matrix composites compressed tested at 700 ^{o}C.

Fig. 9 SEM tensile fractographs of GONs/Ti matrix composites at different magnification. (a) 0wt%, (b) 0.3wt%, (c) 0.6wt% and (d) 0.9wt%, respectively.

Fig. 10 The theoretical calculated strengthening effects of GONs, TiC_x and their combined result versus the reaction fraction of GONs with Ti during SPS.

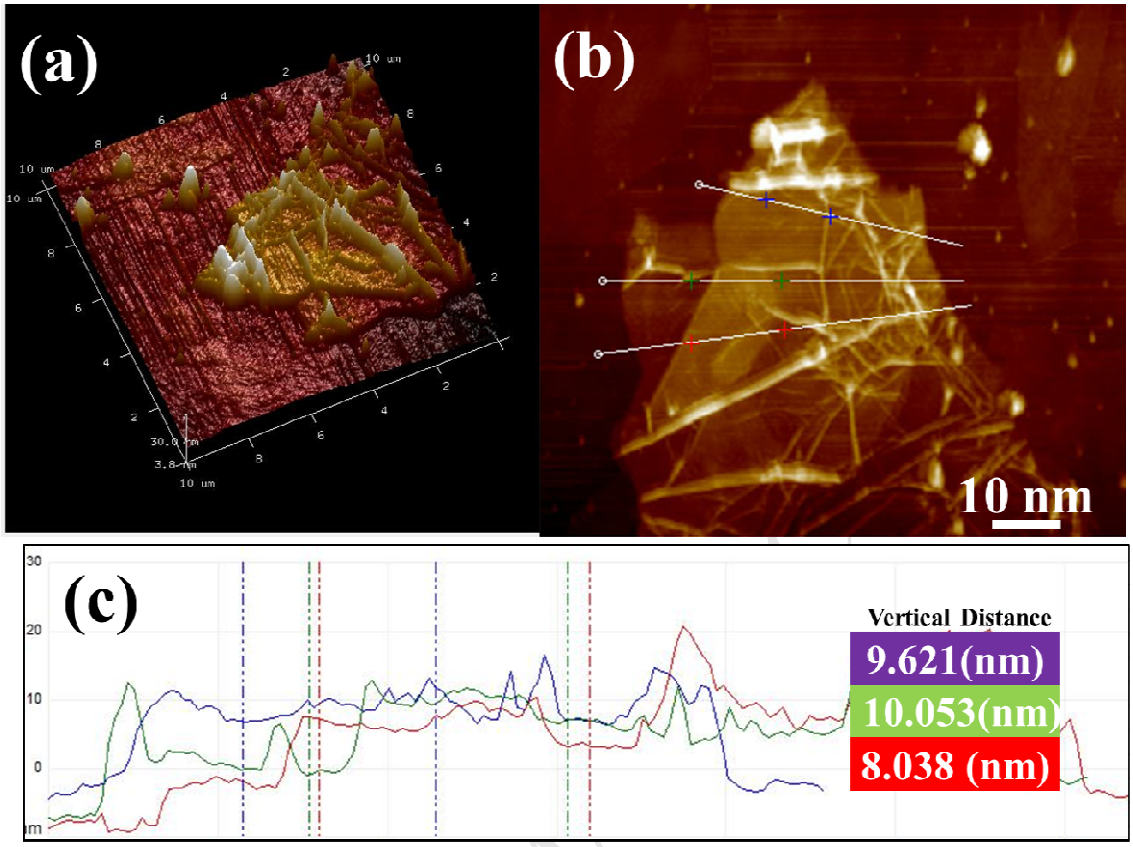

Fig. 1 (a) 3D atom force microscopy (AFM) image of surface morphology; (b) top-view AFM image of as-received GO; and (c) corresponding cross-section height analysis.

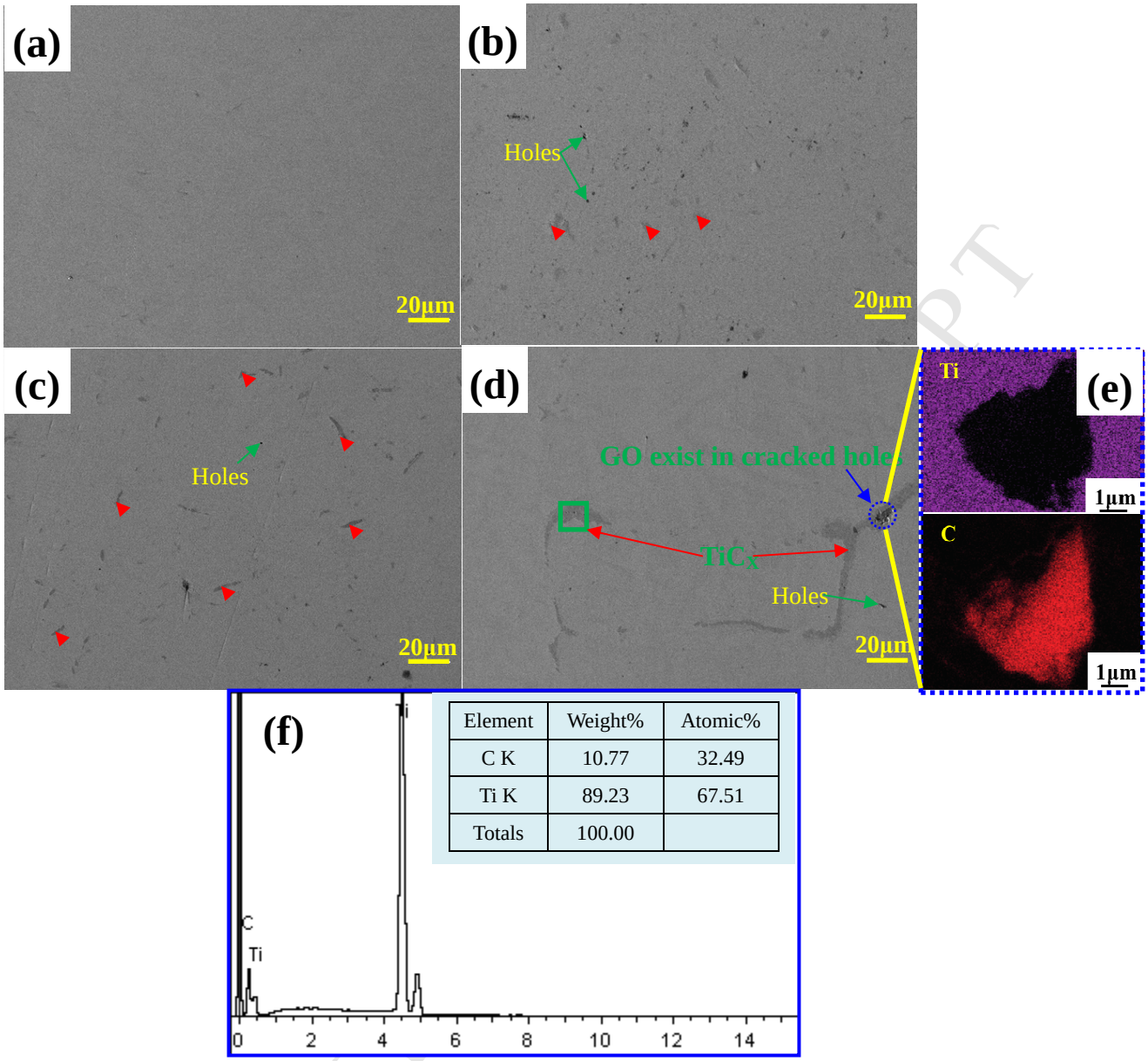

Element	Weight%	Atomic%
C K	10.77	32.49
Ti K	89.23	67.51
Totals	100.00	

Fig. 2 SEM images of Ti matrix composites reinforced with different GONs (a) 0wt%, (b) 0.3wt%, (c) 0.6wt% and (d) 0.9wt%, (f) EDS element analysis of the dark color phase marked in (d), respectively.

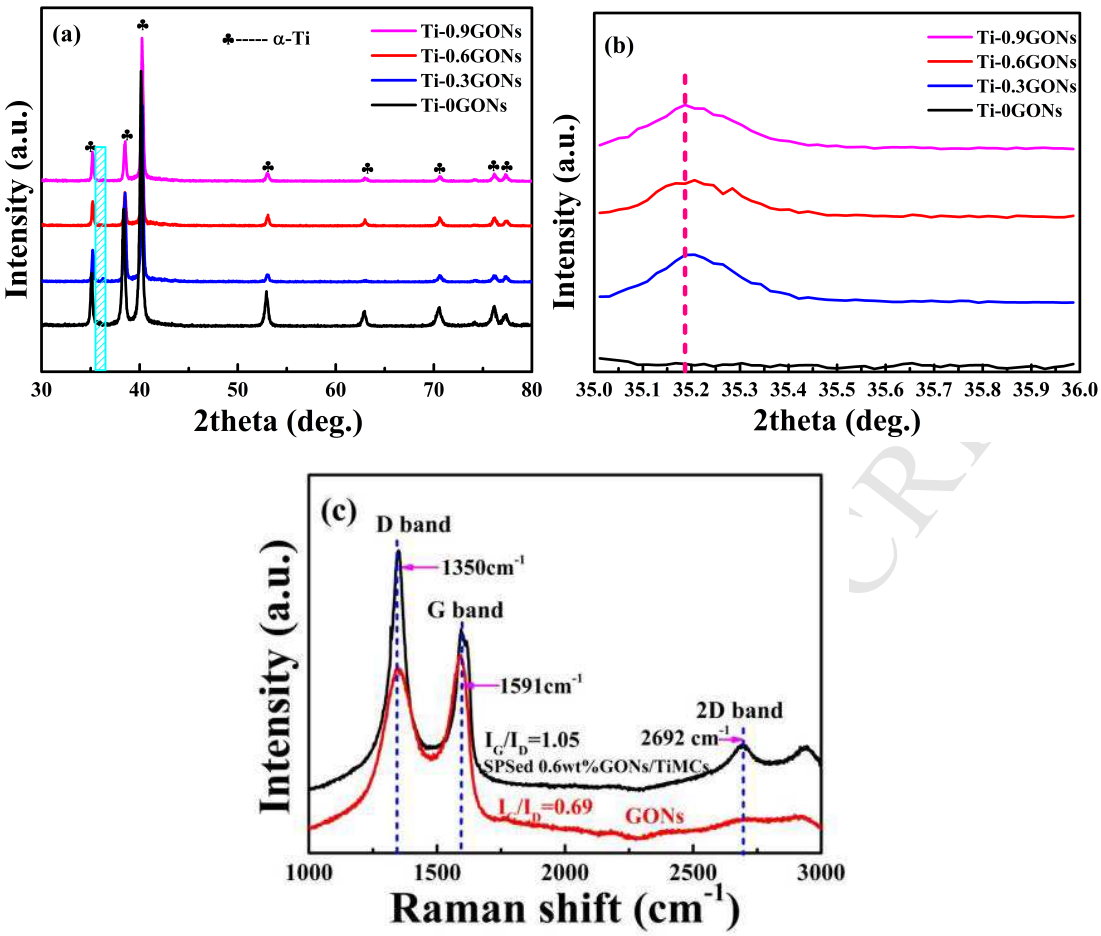

Fig. 3(a) XRD pattern and (b) enlarged region at 2θ = 35.0~36.0° of SPSed Ti matrix composites containing with different GONs, (c) the Raman spectrum of GONs and SPS 0.6wt% GONs/Ti matrix composites.

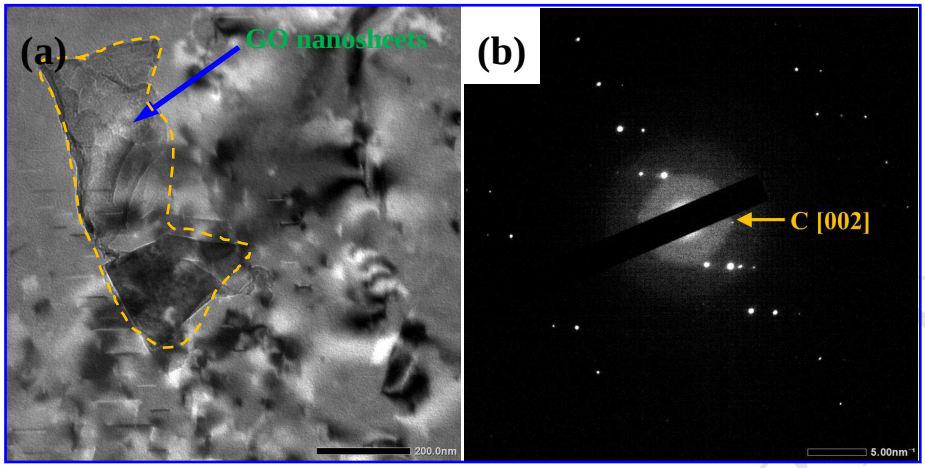

Fig. 4 (a) TEM images and (b) the selected area diffraction pattern (SADP) of 0.3wt%GONs/Ti matrix composites.

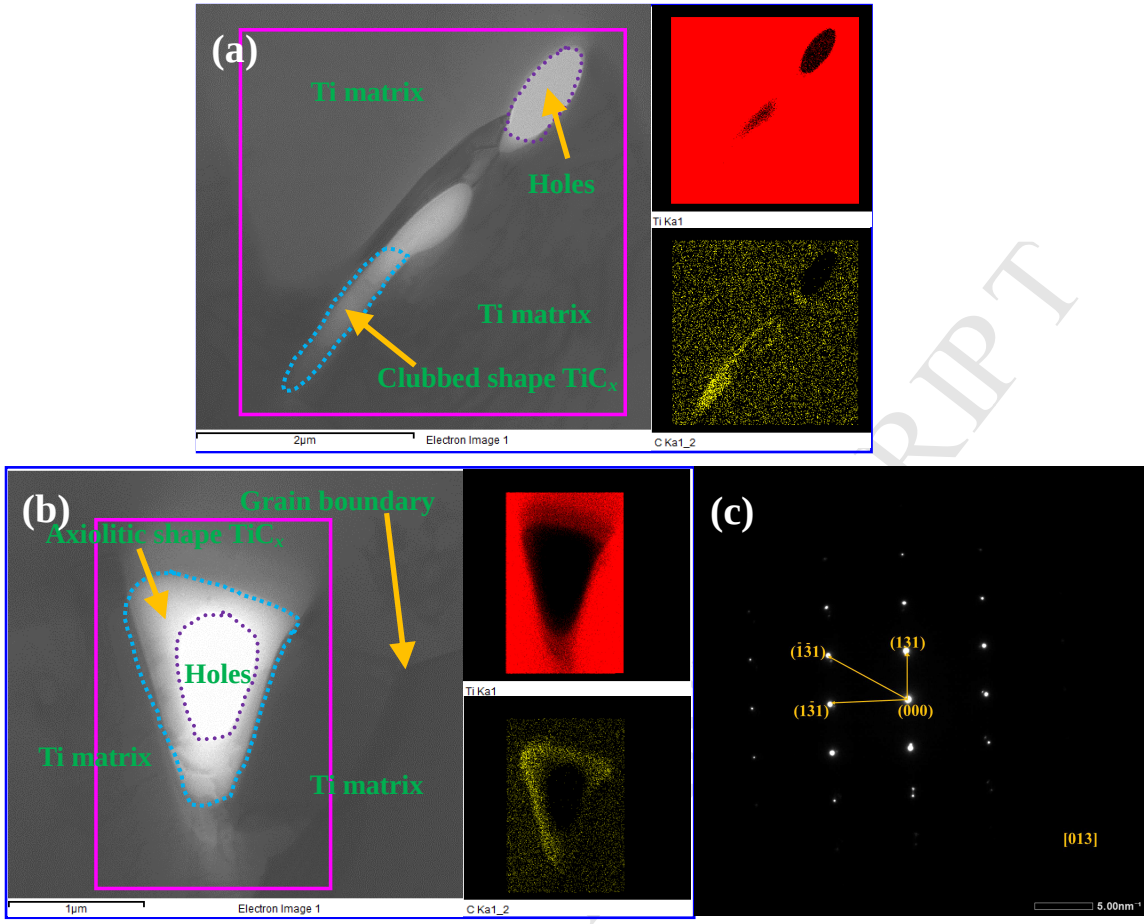

Fig. 5 (a) and (b) TEM, EDS mapping and (c) Selected area diffraction pattern images of 0.9 wt% GONs/Ti matrix composites fabricated by SPS process. (a) and (b) show there are two types of TiC_x particles embedded in the Ti matrix.

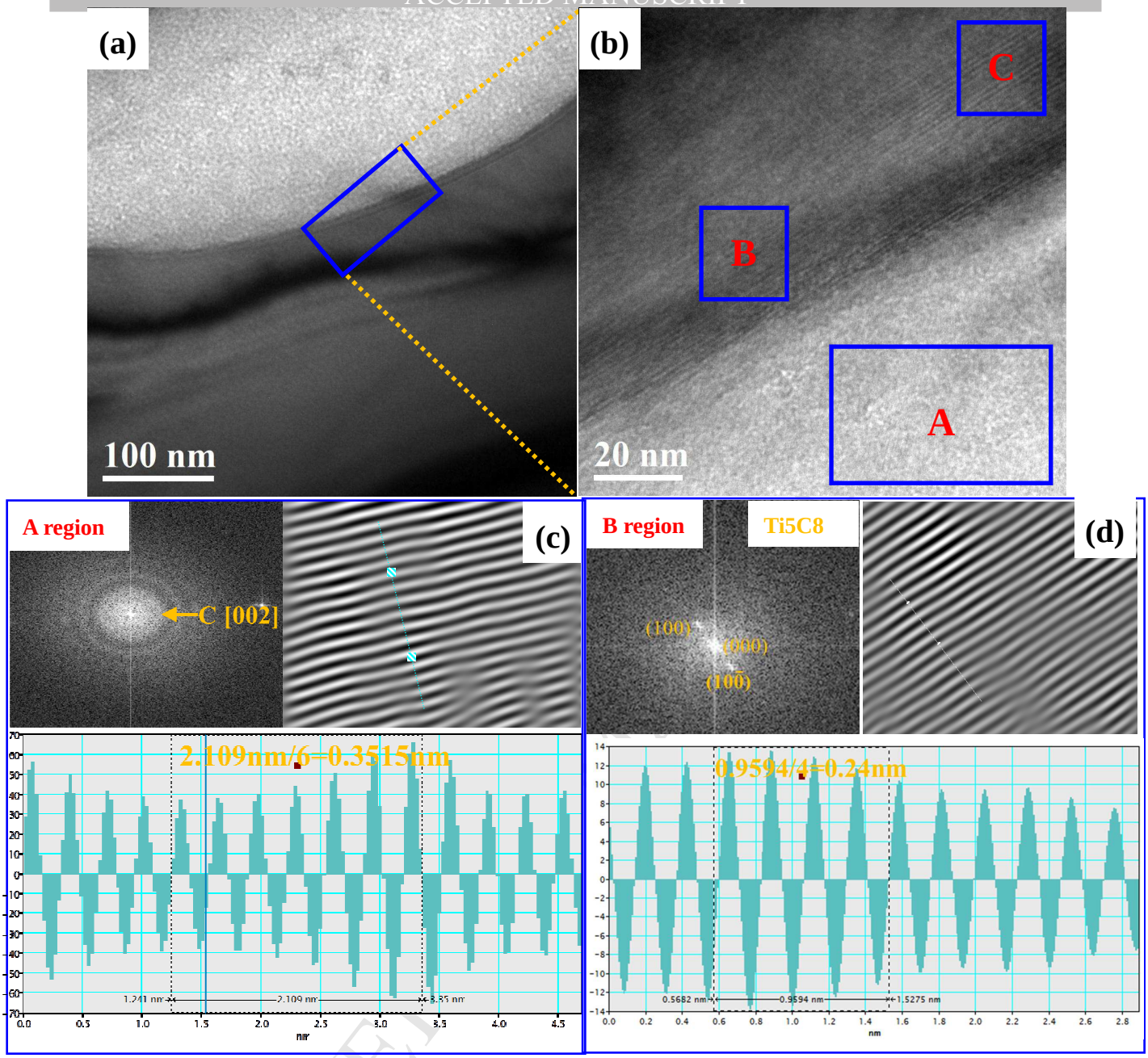
(a)
100 nm
(b)
C
B
A
20 nm
A region
(c)
C [002]
2.109nm/6=0.3515nm
B region
Ti5C8
(d)
(100)
(000)
(100̄)
0.9594/4=0.24nm

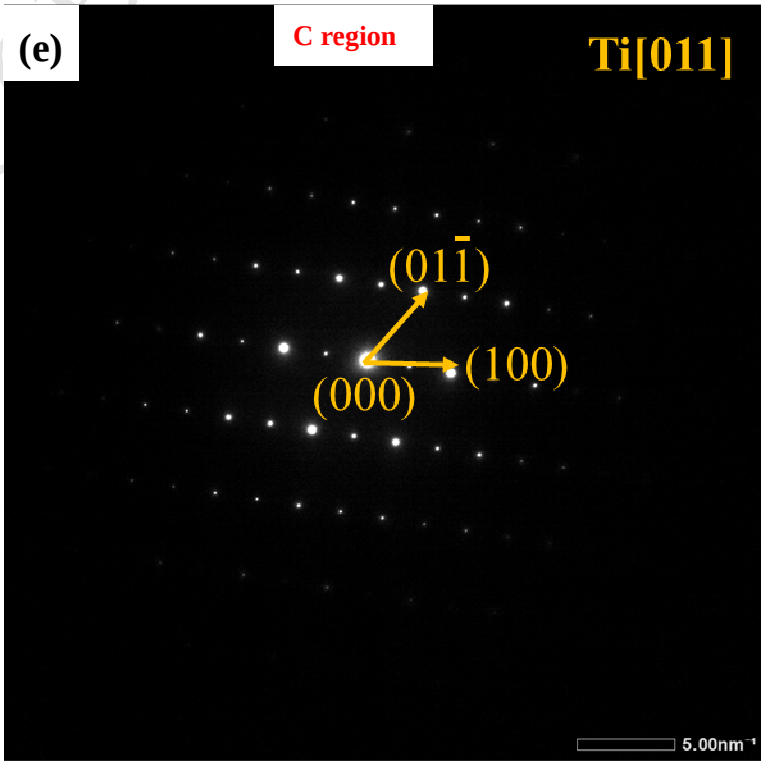
(e)
C region
Ti[011]
(01$\bar{1}$)
(100)
(000)
5.00nm⁻¹

Fig. 6 Detailed analysis and characteristic of interface between Ti matrix and GONs (a) TEM image of GONs/Ti matrix composites, (b) enlarged view image of blue rectangle in (a), (c) and (d) FFT, IFFT and corresponding lattice spacing measurement recorded at the marked A, B regions in (b), respectively, (e) SAED of C region in (b).

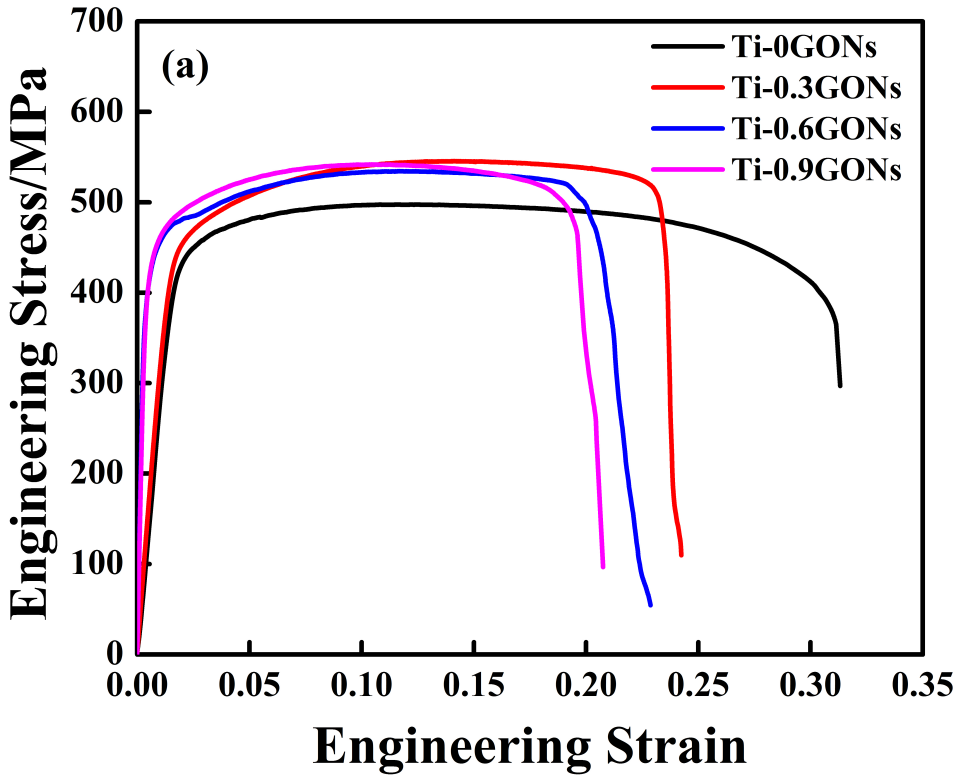
(a)
Ti-0GONs
Ti-0.3GONs
Ti-0.6GONs
Ti-0.9GONs
Engineering Stress/MPa
Engineering Strain
0
100
200
300
400
500
600
700
0.00
0.05
0.10
0.15
0.20
0.25
0.30
0.35

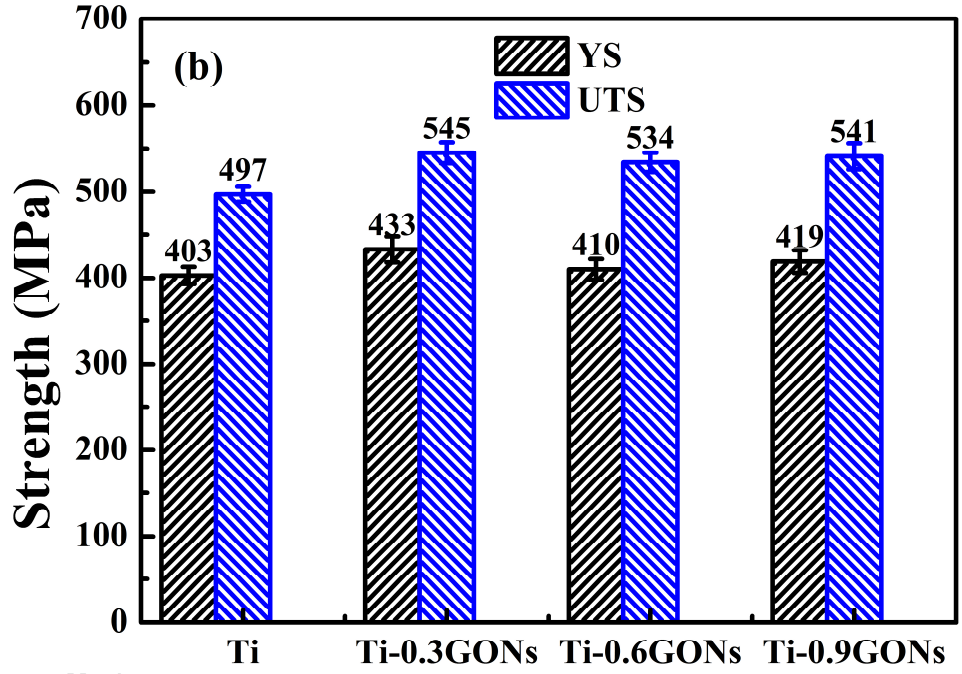
(b)
YS
UTS
Strength (MPa)
403
497
433
545
410
534
419
541
Ti
Ti-0.3GONs
Ti-0.6GONs
Ti-0.9GONs

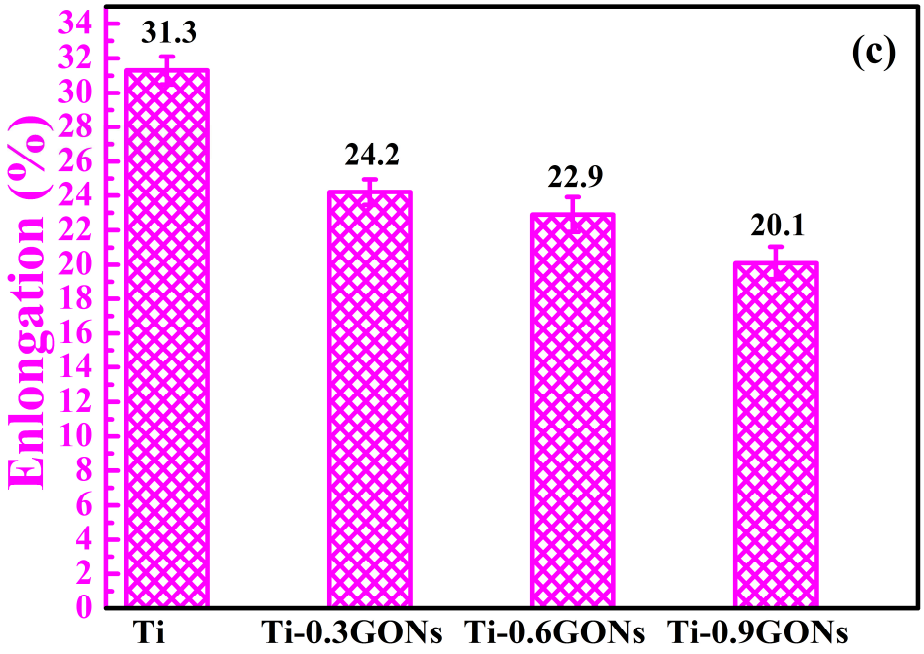

Fig. 7 Room temperature engineering tensile-strain curves and (b) ~ (c) corresponding tensile properties of Ti matrix composites addition of different GONs.

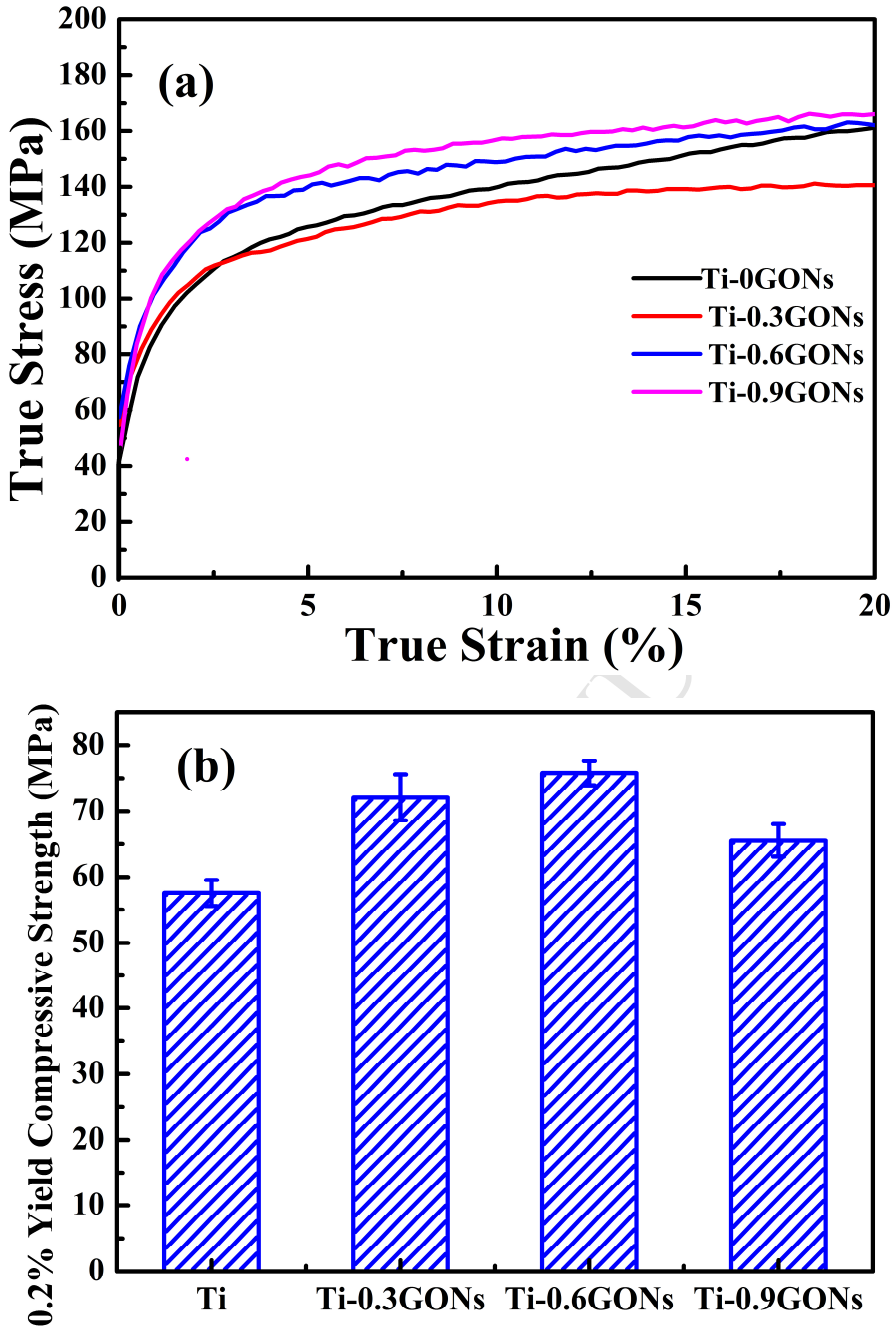

Fig. 8 (a) True stress-strain curves and (b) corresponding compressive strength of Ti matrix composites compressed tested at 700 ^{o}C.

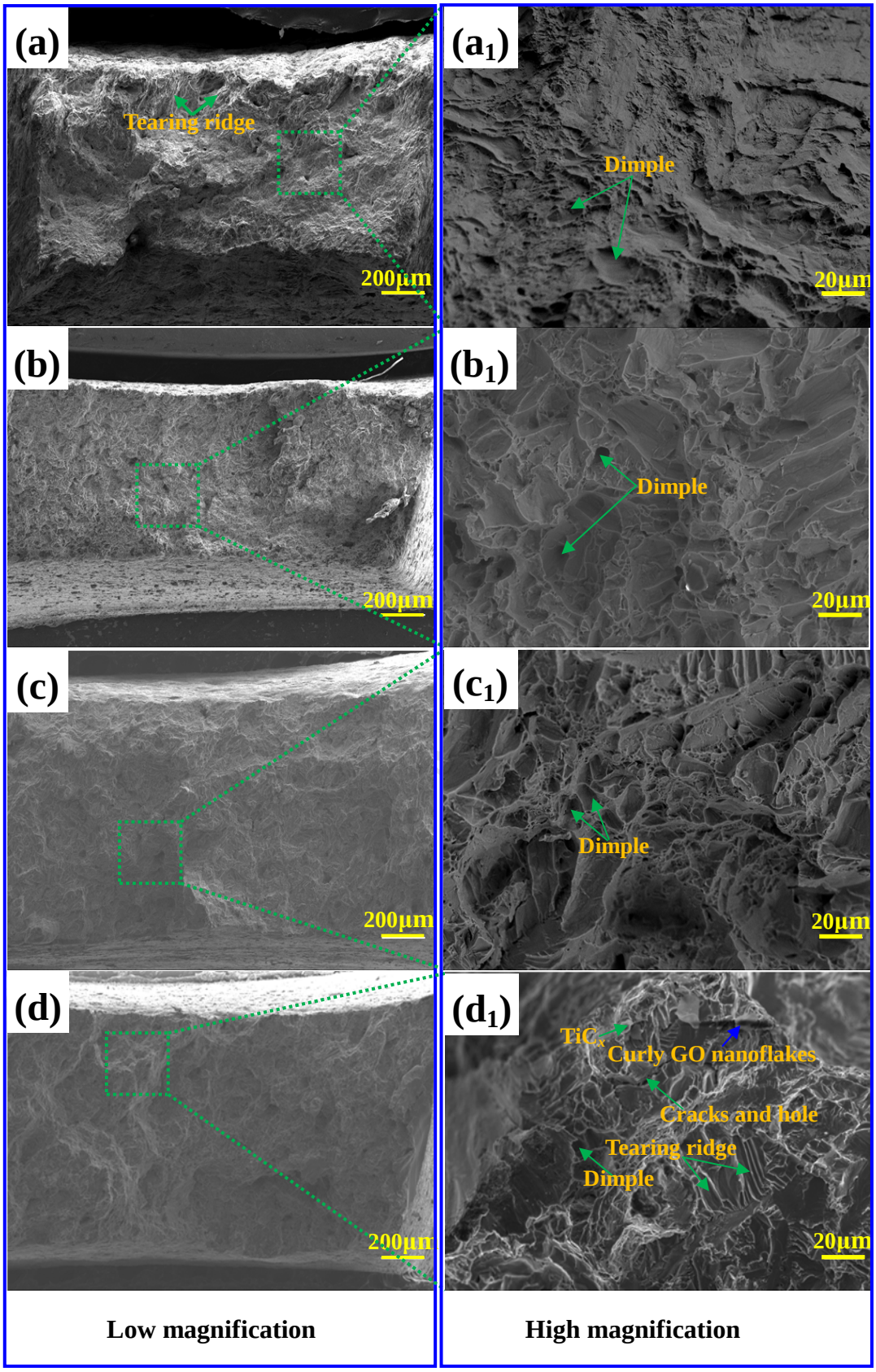

Fig. 9 SEM tensile fractographs of GONs/Ti matrix composites at different magnification. (a) 0wt%, (b) 0.3wt%, (c) 0.6wt% and (d) 0.9wt%, respectively.

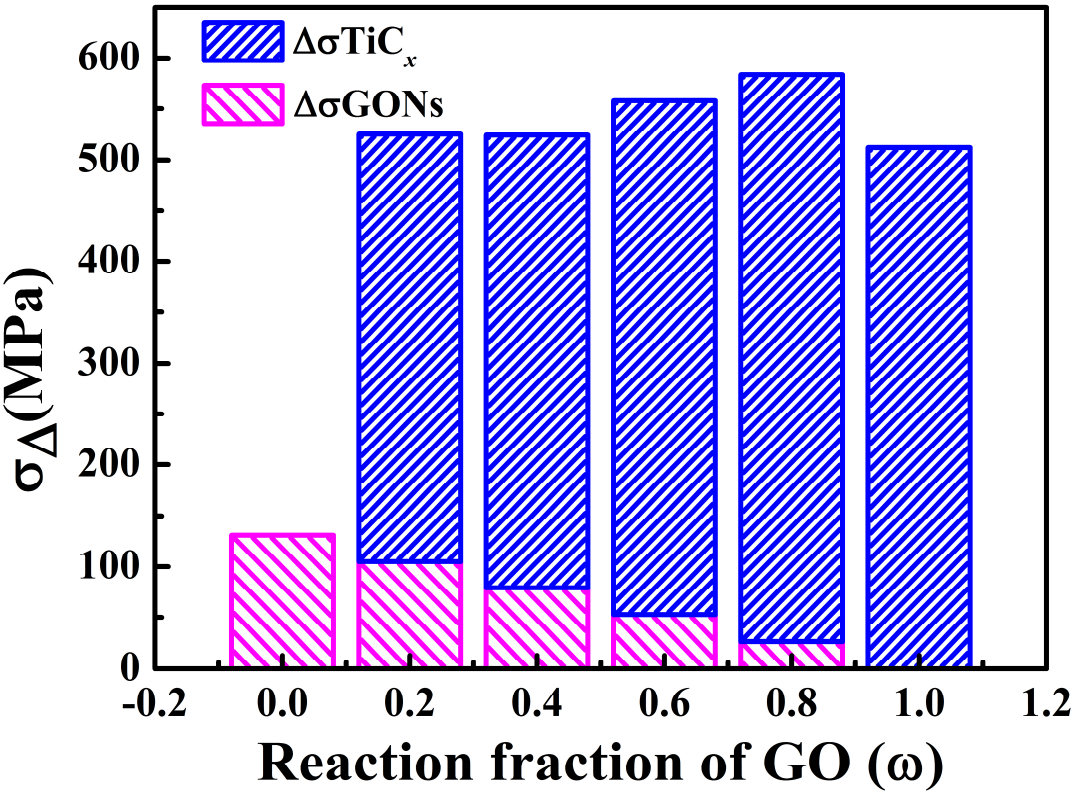

Fig. 10 The theoretical calculated strengthening effects of GONs, TiC_x and their combined result versus the reaction fraction of GONs with Ti during SPS.

List of figure captions:

Table 1 Micro-hardness of GONs/Ti matrix composites sintered at 1100 ^{o}C

Table 1 Micro-hardness of GONs/Ti matrix composites sintered at 1100 ^{o}C

GONs content (wt%)	0	0.3	0.6	0.9
Vickers Hardness (HV)	181.3	203.8	212.9	211.4